ADVANCED MATERIALS
www.advmat.de

Graphene-Network-Backboned Architectures for High-Performance Lithium Storage

Yongji Gong, Shubin Yang, Zheng Liu, Lulu Ma, Robert Vajtai, and Pulickel M. Ajayan**

Lithium ion batteries have gained great success in portable electric devices due to their high energy density, high voltage, and environmental friendliness.[1–9] However, The achievement of lithium ion batteries with excellent electrochemical performances such as high reversible capacity, stable cycle performance, and high rate capability, most important for electric-vehicle applications, is known to be hindered by the lack of suitable electrode materials.[10–12] Thus, various electrochemically active materials made of carbon, metal, metal oxide, and sulfide have been recently developed for lithium storage. In particular, transition metal oxides and sulfides such as Fe_2O_3, Co_3O_4, MoS_2 and WS_2 have shown high reversible capacities (about 1000 mA h g^{-1}) in the initial cycles.[9,13–20] Unfortunately, a large specific volume change commonly occurs in these host matrix during the cycling processes, resulting in pulverization of the electrodes and aggregation of electrode materials. This causes the large increase of contact resistance and rapid capacity decay, especially under high charge and discharge current rates.[6,7]

To circumvent the poor cycle and high-rate problems of transition metal oxides and sulfides, one efficient strategy is to find suitable matrix to accommodate their volume change during the cycle processes.[21] In this respect, a variety of carbonaceous materials such as porous carbons, carbon nanotubes, and graphene have been synthesized for loading of metals, metal oxides, and sulfides.[14,22–26] Among them, graphene is the most promising matrix due to the high electrical conductivity, good flexibility, and high chemical stability.[17,20] Hence, some metal oxide and sulfide-graphene hybrids such as MnO_x-graphene, Co_3O_4-graphene, and MoS_2-graphene have been developed.[22–24] To date, they can be mainly divided into two categories according to their different structures: directly mixed metal oxide or sulfide-graphene composites and sandwich-like, graphene-supported hybrid nanosheets.[17,22–24] Although improved electrochemical performances have been observed, some disadvantages for lithium storage still exist in these hybrids. For the former, the metal oxides and sulfides are still prone to strong aggregation during the cycle processes due to the non-intimate contact between the graphene layers and the active materials, and the latter suffers from the large contact resistance among numerous active nanosheets. Thus, the achievement of metal oxide or sulfide-graphene hybrids with superior electrochemical performances remains a big challenge.

Very recently, graphene oxide (GO) aerogels and hydrogels with 3D porous interconnected frameworks and large specific surface area have been developed and used for energy storage.[27–29] Here, we demonstrate an efficient approach to large-scale fabrication of various three-dimensional (3D) graphene-backboned hybrid architectures including MoS_2/graphene and FeO_x/graphene via a hydrothermal method. The resulting graphene-backboned architectures possess high surface area, porous structure, and continuous graphene backbone. These features not only facilitate the easy access of an electrolyte, and fast diffusion of electrons, but also can accommodate the volume change of metal oxides and sulfides, and prevent their aggregation during cycle processes. As a result, the high reversible capacity, ultrahigh-rate capability, and excellent cycle performance are achieved for graphene-backboned hybrid architectures.

As illustrated in **Figure 1**a, 3D graphene-backboned hybrid architectures were fabricated by a simple hydrothermal approach (for details, see Experimental Section). Reduction of $(NH_4)_2MoS_4$ with NH_2NH_2 and hydrolysis of $FeCl_3$ were chosen to grow MoS_2 and FeO_x atomic layers in situ onto the surface of GO. These reactions were carried out at 180 °C in the presence of GO in aqueous solution, where GO was chemically reduced to graphene (or reduced graphene oxide), to generate MoS_2 or FeO_x-graphene architectures simultaneously. Notably, the weight fractions of MoS_2 or FeO_x in the as-prepared 3D architectures were facilely controlled by adjusting the ratios between the metal salts and the GO. In this text, all the contents of MoS_2 and FeO_x were calculated on the basis of weight fraction (wt%). The typical photographs of MoS_2-graphene and FeO_x-graphene architectures (Figure 1b) demonstrate clearly the centimeter-scale columned shape with low volume densities (≈50 mg cm^{-3}).

The 3D architectures built by flexible nanosheets in the as-prepared MoS_2/graphene and FeO_x/graphene samples were firstly confirmed by field-emission scanning electron microscopy (FE-SEM). As shown in Figure 1c, the morphologies of the as-prepared 3D architectures are similar to those reported for grpahene and graphene oxide hydrogels.[27,28] The porous nature of MoS_2/graphene and FeO_x/graphene architectures is then demonstrated by the nitrogen physisorption measurements (Figure 1d). Their adsorption-desorption isotherms exhibit a typical IV hysteresis loop at a relative pressure between 0.6 and 0.9, characteristic of pores with different pore sizes. Barrett–Joyner–Halenda (BJH) calculations disclose that

Y. J. Gong, Prof. P. M. Ajayan
Department of Chemistry
Rice University
6100 Main Street, 77005, Houston, USA
E-mail: ajayan@rice.edu
Dr. S. B. Yang, Z. Liu, L. L. Ma, R. Vajtai,
Prof. P. M. Ajayan
Department of Mechanical Engineering & Materials Science
Rice University
6100 Main Street, 77005, Houston, USA
E-mail: shubin.yang@rice.edu

DOI: 10.1002/adma.201301051

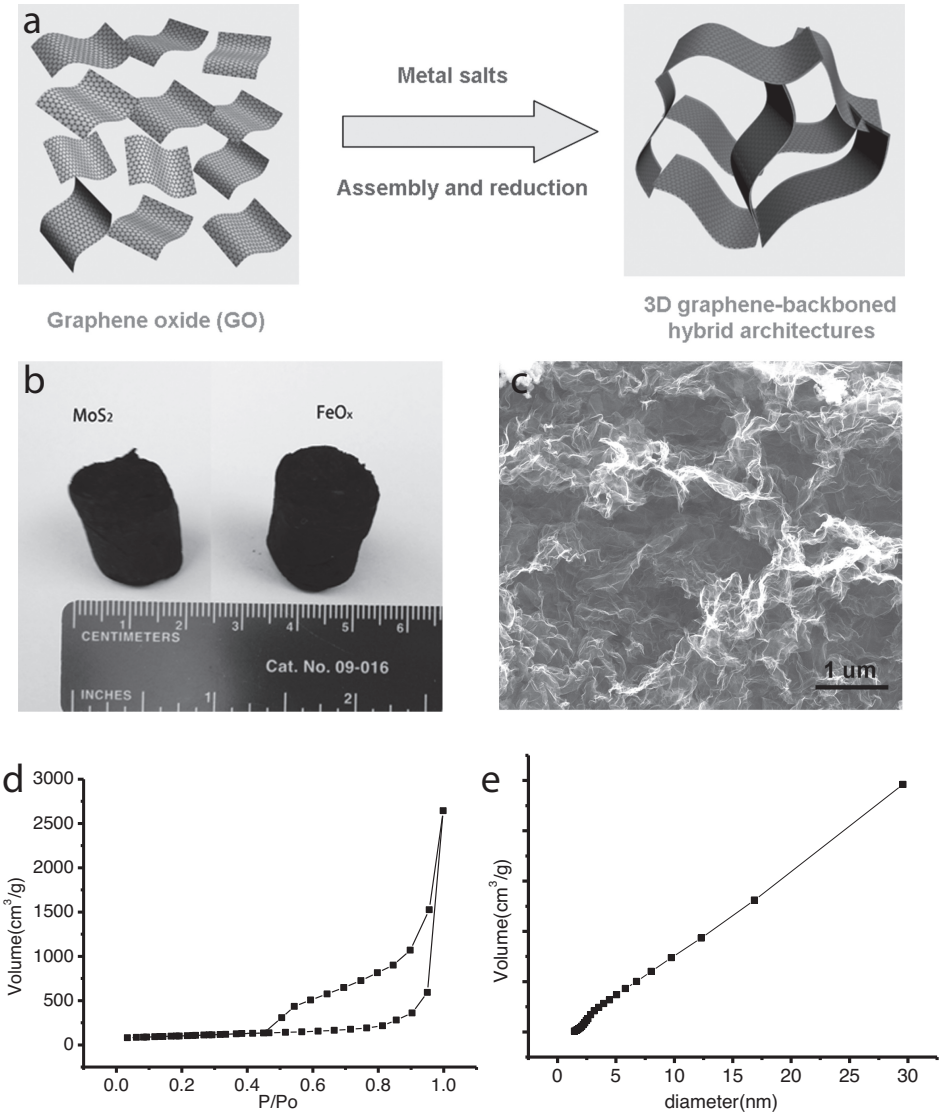

Figure 1. Fabrication of 3D graphene-backboned architecture. a) Schematic diagram for the fabrication of 3D MoS_2-graphene architectures by a simple hydrothermal method. b) Typical photograph of obtained architecture shows the centimeter scale size. c) Typical SEM images of 3D MoS_2-graphene or FeO_x-graphene architectures reveal the thin and continuous walls. d) Nitrogen adsorption/desorption isotherms of MoS_2/graphene architecture (85%) confirms the porous structure with a high BET surface area of 285 m^2 g^{-1}. e) Pore-size distribution reveals that the pore sizes in MoS_2-graphene architectures are in the range of 3–30 nm.

the pore size distribution is in the range of 3–30 nm, except for the open macropores revealed from the SEM images, as shown in Figure 1e. The adsorption data indicate specific surface areas of 285 and 265 m^2 g^{-1} for the MoS_2/graphene and FeO_x/graphene architectures, respectively, with the same active material content of 85%.

The microstructure of as-prepared MoS_2/graphene architectures was then investigated by transmission electron microscopy (TEM) and high-resolution TEM (HRTEM). As presented in **Figure 2**a, the thin and continuous building blocks, nanosheets, for 3D MoS_2-graphene architectures are visible. Cross-sectional atomic force microscopy (AFM) images and thickness analyses (Supporting Information, Figure S1) reveal the same nanosheet morphology with uniform thickness of ≈2–3 nm. The typical HRTEM image (Figure 2b) further discloses the hexagonal crystalline lattice of MoS_2 on the surface of graphene sheets. Coupled with their elemental mapping analysis, the homogeneous distribution of MoS_2 on graphene is distinctly observed as shown in Figure 2d, where the black and grey colors stand for sulfur and carbon, respectively. To gain further insight into the elemental analysis, we performed the X-ray photoelectron spectroscopy (XPS) of MoS_2-graphene architectures with different MoS_2 contents (85% and 65%) (Supporting Information, Figure S2). An atomic ratio of ≈1/2 between Mo and S for all the MoS_2/graphene samples is achieved (Supporting Information, Figure S2a–S2c), well consistent with that of commercially available bulk MoS_2. Moreover, two symmetrical XPS peaks are presented at the same binding energy to bulk MoS_2, indicating the formation of MoS_2

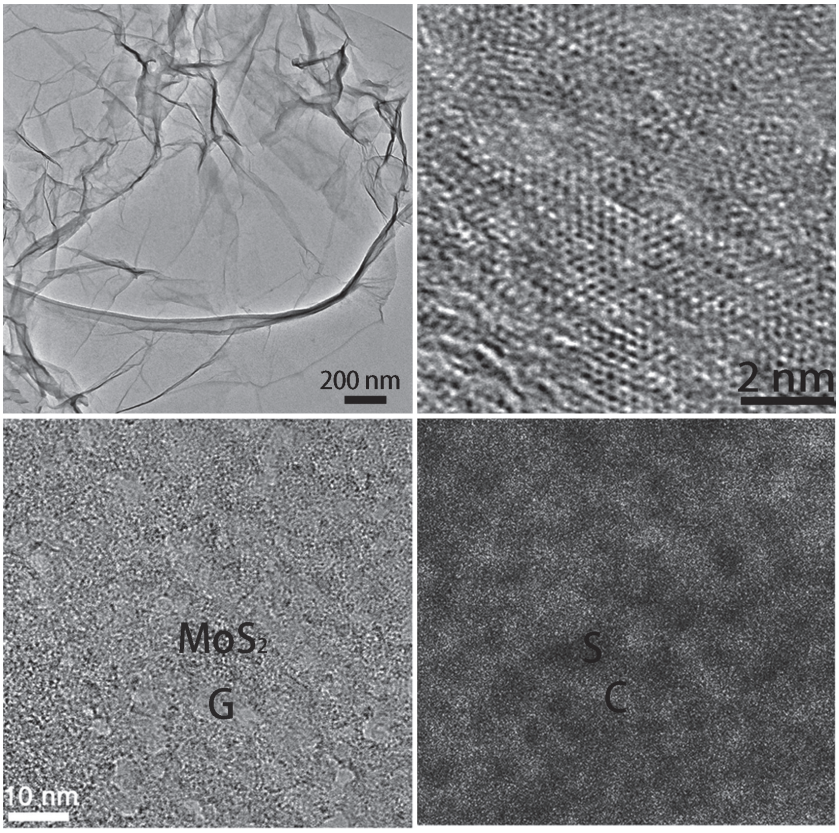

Figure 2. The building blocks, MoS_2/graphene sheets, for 3D MoS_2/graphene architectures. a) Typical TEM image of MoS_2-graphene architecture (85%), showing that continuous thin MoS_2/graphene hybrid walls. b) HRTEM image of a typical sheet of MoS_2/graphene architecture (85%), showing the hexagonal crystal structure of MoS_2. c,d) STEM image of the MoS_2/graphene structure and its corresponding S and C element mapping, where black stands for sulfur and grey stands for carbon.

layers during our hydrothermal process. This is further demonstrated by their Raman and X-ray diffraction (XRD) analysis of MoS_2-grpahene architectures (Supporting Information, Figure S3,S4). For the Raman spectra, in addition to peaks of GO, there are peaks consistent with the Raman spectra of bulk MoS_2. All the XRD peaks are indexed in the space group P63/mmc MoS_2 with a hexagonal structure (JCPDS No. 37–1492).

Meanwhile, 3D FeO_x/graphene architectures with a similar morphology to that of MoS_2/graphene architectures are obtained (Supporting Information, Figure S5). The biggest differences between them lie in the thickness and crystalline structure of their building walls. As analyzed by AFM (Supporting Information, Figure S6), the thickness of the FeO_x/graphene sheets is ≈4–5 nm, slightly thicker than that of the MoS_2/graphene sheets (2–3 nm). The typical HRTEM image (Supporting Information, Figure S5d) reveals the amorphous FeO_x layers on graphene in the case of FeO_x/graphene architectures. To gain insight into the elemental composition, we performed XPS analysis of the FeO_x/graphene architectures with different FeO_x contents (Supporting Information, Figure S7). XPS spectra of high-resolution Fe3d5/2, O1s, and C1s disclose that the obtained FeO_x have very similar peak positions to commercially available Fe_3O_4.

The electrochemical performances of 3D MoS_2/graphene architectures were systematically evaluated by galvanostatic discharge (lithium insertion)–charge (lithium extraction) measurements at various rates (*n*C), where *n*C corresponds to the full lithium extraction from electrodes in 1/*n* h. Remarkably, a very high reversible capacity of about 1200 mA h g^{-1} is achieved in the initial cycles at 0.5C (600 mA g^{-1}), in the case of MoS_2-graphene architecture with the MoS_2 content of 85% (**Figure 3**b). Although the Coulombic efficiency (the ratio between charge capacity and discharge capacity) is only 68% in the initial cycle, it rapidly reaches more than 99% after the second cycle. Even after 30 cycles, both the discharge and charge capacities of this architecture are stable at about 1200 mA h g^{-1}, delivering nearly 100% capacity retention. When the MoS_2 content decreases to 65%, the reversible capacity decreases correspondingly to ≈800 mA h g^{-1} but with the same stable cycle performance. These results are in stark contrast to that of the MoS_2 particles obtained by the same synthesis process only without GO, which show continuous and progressive capacity decay to 80 mA h g^{-1} under the same testing conditions. Moreover, the MoS_2/graphene architectures exhibit excellent rate performances. As shown in Figure 3c, high reversible capacities of 620 and 270 mA h g^{-1} are achieved at 12C and 140C (the corresponding full charge or discharge times are 5 min and 25 s), respectively, in the case of MoS_2-graphene architecture with the MoS_2 content of 85%. Most importantly, this architecture exhibits very stable cycle performance at various charge–discharge rates. As shown in Figure 3d, no capacity decay is observed, even after 3000 cycles, at any of the selected rates, 12C, 43C and 140C. This is significantly different from those reported for MoS_2-based materials.[9,23,24] To the best of our knowledge, our 3D MoS_2-graphene architecture is one of the most promising anode materials reported for lithium storage.

In the case of anode materials with excellent high-rate performances, the electrochemical performance at high temperature is also very important for practical batteries. Thus, we investigated the electrochemical performances of the MoS_2/graphene architectures at various selected temperatures, such as 25 °C, 50 °C, and 75 °C. As shown in Figure S8 in the Supporting Information, on increasing the environmental temperature from 25 to 75 °C, the reversible capacity clearly increases from 1000 to 1150 mA h g^{-1} at a current rate of 1C. The enhanced capacity should be attributed to the significantly enhanced diffusion rates of lithium ions in the electrodes at high temperatures. Moreover, the MoS_2/graphene architecture exhibits a stable cycle performance at the high temperatures. To gain insight into the reason that the 3D MoS_2/graphene architecture possesses such excellent electrochemical

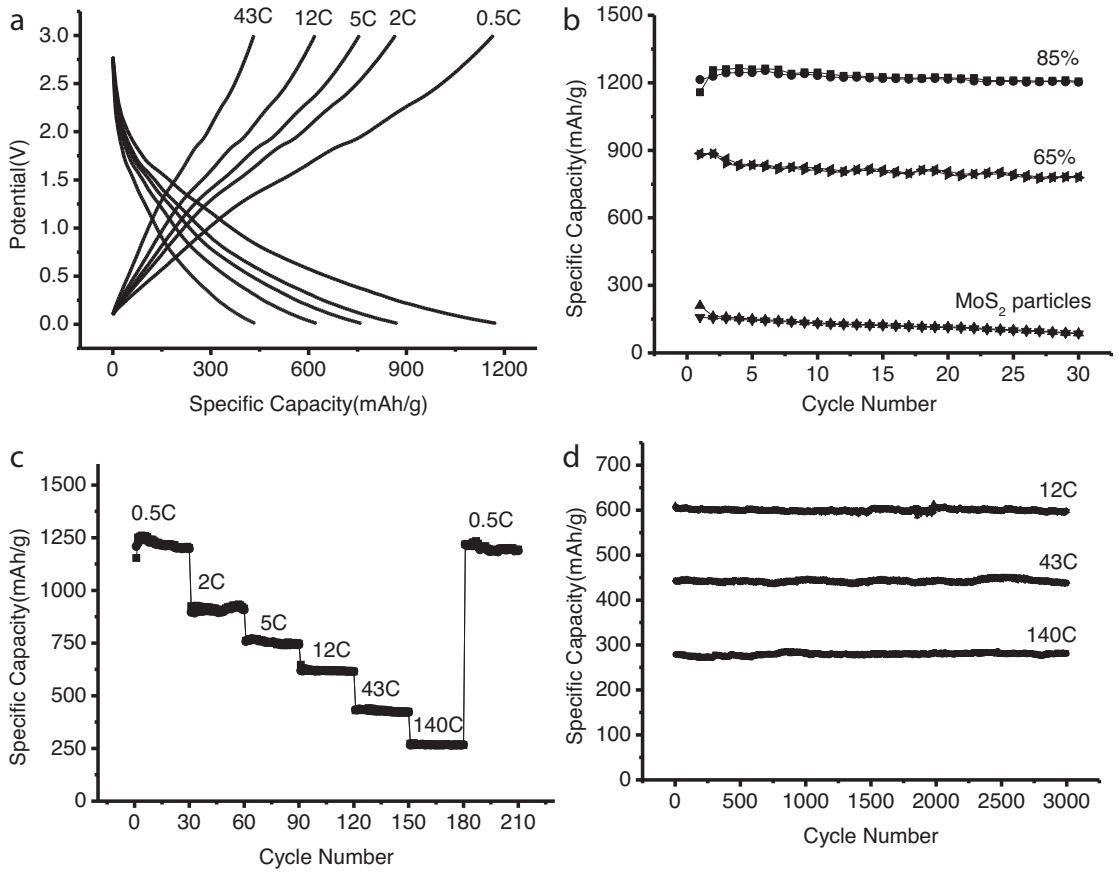

Figure 3. Electrochemical performance of 3D MoS_2/graphene architectures. a) Representative discharge–charge curves of MoS_2/graphene (85%) architecture at various C-rates. b) Different cycle performance of MoS_2/graphene (85%), MoS_2/graphene (65%) and MoS_2 particles at current density of 0.5C (600 mA g^{-1}). c) Rate capacities of MoS_2-graphene architectures with 85% MoS_2 contents. d) Capacity retentions of MoS_2/graphene (85%) architecture when performing full discharge–charge for 3000 cycles. From up to down, the curves are denoted as charge and discharge rates of 12C, 43C, and 140C, respectively.

performances for lithium storage, we performed electrochemical impedance measurements for the MoS_2-graphene architecture (85%) and pure MoS_2 nanosheets. As shown in Figure S9 in the Supporting Information, Nyquist plots show that the diameter of the semicircle for the 3D MoS_2-graphene architecture (85%) in the high–medium frequency region is much smaller than that of pure MoS_2 nanosheets, which suggests that MoS_2-graphene architecture possess much lower contact and charge-transfer resistances. This result clearly validates that our graphene-network backboned strategy can not only improve the high conductivity of the overall electrode, but also largely enhance the electrochemical activity of the MoS_2 during the cycle processes.

Similarly excellent electrochemical performances can be also achieved from the 3D FeO_x/graphene architectures. As shown in **Figure 4**, a high reversible capacity of 1100 mA h g^{-1} is obtained at 0.5C for the FeO_x/graphene architecture with the FeO_x content of 85%. Although this value is slightly lower than that of MoS_2-graphene architecture (1200 mA h g^{-1}), it is much higher than that of FeO_x produced by the same procedure only without GO (70 mA h g^{-1}). Moreover, the FeO_x-graphene architecture delivers similar fast rate capability and excellent cycle performance to those of the MoS_2-graphene architectures. For instance, at 80C (corresponding total charge and discharge time is 45 s), the reversible capacity is stable at 270 mA h g^{-1} even after 1500 cycles. This is totally different from those reported for various iron oxides, which show a clear capacity loss within 100 cycles.[20,21] Such excellent results shed light on the utility of graphene-backboned architectures to improve the electrochemical performance of a variety of metals, metal oxides, and sulfides.

In summary, we have designed 3D porous architectures constructed by graphene sheets coated with MoS_2 or FeO_x for high-performance battery materials, without any other additives. Stable battery electrodes with a long cycle life (3000 cycles for MoS_2 and 1500 cycles for FeO_x with almost 100% capacity retention) at different charge and discharge rates were achieved as they were used for lithium storage. In addition, their specific capacity can be up to 1100–1200 mA h g^{-1} at 0.5C. Furthermore, the excellent rate capabilities for MoS_2/graphene and FeO_x/graphene can be up to 140C and 80C, respectively. Their performances are very promising for the next generation of high-performance batteries for portable electronics, electric vehicles, and hybrid vehicles.

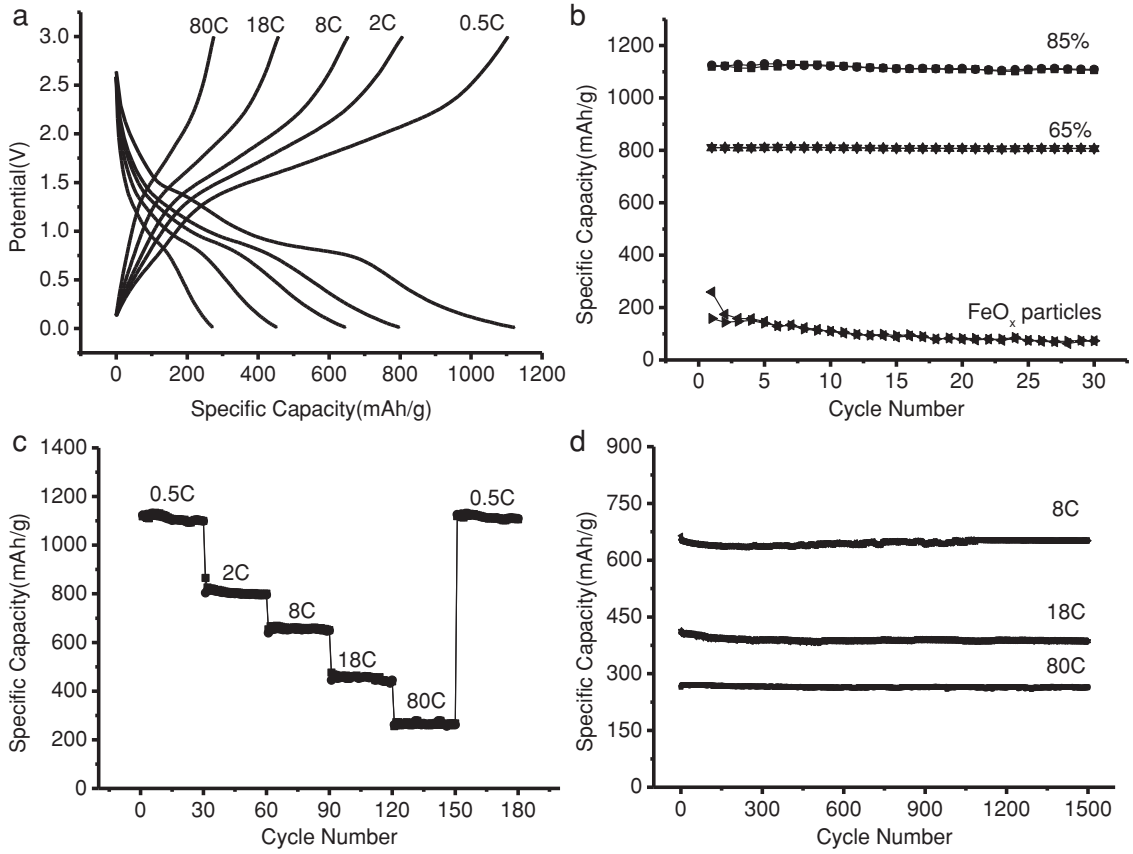

Figure 4. Electrochemical performance of 3D FeO_x/graphene architectures. a) Representative discharge–charge curves of FeO_x/graphene (85%) architecture at various C-rates. b) Different cycle performance of FeO_x/graphene (85%), FeO_x/graphene (60%) and FeO_x particles at 0.5C (550 mA g^{-1}). c) Rate capacities of FeO_x/graphene architectures with 85% FeO_x contents. d) Capacity retentions of FeO_x/graphene (85%) architecture when performing full discharge–charge for 1500 cycles. From up to down, the curves are denoted as charge and discharge rates of 8C, 18C, and 80C, respectively.

Experimental Section

Graphene oxide (GO) nanosheets were synthesized from natural graphite flakes by a modified Hummers method, the details of which are described elsewhere.[25] 3D MoS_2/graphene or FeO_x/graphene architectures were synthesized by a simultaneous hydrothermal synthesis and assembly procedure. In a typical procedure, a 5 mL of GO (2 mg mL^{-1}) aqueous dispersion were mixed with different amounts of commercially available $(NH_4)_2MoS_4$ or $FeCl_3{\cdot}6H_2O$ powder by sonication for 10 min. To get the MoS_2/graphene architecture, hydrazine is necessary as a reducing agent. The resulting mixture was then sealed in a polytetrafluoroethylene (Telfon)-lined autoclave, and was hydrothermally treated at 180 °C for 6 h. Finally, the as-prepared samples were chemically reduced and freeze- or critical-point-dried to preserve the 3D architectures formed during the synthesis process. The exact weight fractions of MoS_2 or FeO_x in the architectures were calculated by subtracting the weight of added GO from the weight of the dried architectures.

The morphology and microstructure of the samples were systematically investigated by FE-SEM (JEOL 6500), TEM (JEOL 2010), HRTEM (Field Emission JEOL 2100), AFM (Digital Instrument Nanoscope IIIA), XPS (PHI Quantera x-ray photoelectron spectrometer), and XRD (Rigaku D/Max Ultima II Powder X-ray diffractometer) measurements. Raman spectroscopy (Renishaw in Via) was performed at 514.5 nm laser excitation at a power of 20 mW. Nitrogen sorption isotherms and the BET surface area were measured at 77 K using a Quantachrome Autosorb-3B analyzer (USA). Electrochemical experiments were carried out in 2032 coin-type cells. The as-prepared MoS_2/graphene monoliths or architectures were directly fabricated as binder/additive-free working electrodes by cutting then into small thin round slices with a thickness of ≈1 mm and processing into these slices into thinner electrodes upon pressing. Pure lithium foil (Aldrich) was used as the counter electrode. The electrolyte consisted of a solution of 1 M $LiPF_6$ in ethylene carbonate (EC)/dimethyl carbonate (DMC)/diethyl carbonate (DEC) (1:1:1 by volume) obtained from MTI Corporation. The cells were assembled in an argon-filled glove box with the concentrations of moisture and oxygen below 0.1 ppm.

Supporting Information

Supporting Information is available from the Wiley Online Library or from the author.

Acknowledgements

This work was financially supported by U.S. Army Research Office through a MURI grant (W911NF-11-1-0362) on Novel Free-Standing 2D

Crystalline Materials focusing on Atomic Layers of Nitrides, Oxides, and Sulfides and the U.S. Office of Naval Research MURI grant (N000014-09-1-1066) on graphene. S.Y. and P.M.A. also acknowledge funding sponsorship from the U.S. Department of Defense: U.S. Air Force Office of Scientific Research for the Project MURI: "Synthesis and Characterization of 3-D Carbon Nanotube Solid Networks" award no.: FA9550-12-1-0035.

Received: March 7, 2013
Revised: April 26, 2013
Published online: June 13, 2013

[1] B. Kang, G. Ceder, *Nature* **2009**, *458*, 190.
[2] K. S. Kang, Y. S. Meng, J. Breger, C. P. Grey, G. Ceder, *Science* **2006**, *311*, 977.
[3] M. Morcrette, P. Rozier, L. Dupont, E. Mugnier, L. Sannier, J. Galy, J. M. Tarascon, *Nat. Mater.* **2003**, *2*, 755.
[4] M. Armand, S. Grugeon, H. Vezin, S. Laruelle, P. Ribiere, P. Poizot, J. M. Tarascon, *Nat. Mater.* **2009**, *8*, 120.
[5] N. Recham, J. N. Chotard, L. Dupont, C. Delacourt, W. Walker, M. Armand, J. M. Tarascon, *Nat. Mater.* **2010**, *9*, 68.
[6] H. Wu, G. Chan, J. W. Choi, I. Ryu, Y. Yao, M. T. McDowell, S. W. Lee, A. Jackson, Y. Yang, L. B. Hu, Y. Cui, *Nat. Nanotechnol.* **2012**, *7*, 309.
[7] C. K. Chan, H. L. Peng, G. Liu, K. McIlwrath, X. F. Zhang, R. A. Huggins, Y. Cui, *Nat. Nanotechnol.* **2008**, *3*, 31.
[8] K. T. Nam, D. W. Kim, P. J. Yoo, C. Y. Chiang, N. Meethong, P. T. Hammond, Y. M. Chiang, A. M. Belcher, *Science* **2006**, *312*, 885.
[9] H. Hwang, H. Kim, J. Cho, *Nano Lett.* **2011**, *11*, 4826.
[10] H. G. Zhang, X. D. Yu, P. V. Braun, *Nat. Nanotechnol.* **2011**, *6*, 277.
[11] A. S. Arico, P. Bruce, B. Scrosati, J. M. Tarascon, W. Van Schalkwijk, *Nat. Mater.* **2005**, *4*, 366.
[12] P. G. Bruce, B. Scrosati, J. M. Tarascon, *Angew. Chem. Int. Ed.* **2008**, *47*, 2930.
[13] Y. J. Lee, H. Yi, W. J. Kim, K. Kang, D. S. Yun, M. S. Strano, G. Ceder, A. M. Belcher, *Science* **2009**, *324*, 1051.
[14] A. Magasinski, P. Dixon, B. Hertzberg, A. Kvit, J. Ayala, G. Yushin, *Nat. Mater.* **2010**, *9*, 353.
[15] B. L. Ellis, W. R. M. Makahnouk, Y. Makimura, K. Toghill, L. F. Nazar, *Nat. Mater.* **2007**, *6*, 749.
[16] P. Poizot, S. Laruelle, S. Grugeon, L. Dupont, J. M. Tarascon, *Nature* **2000**, *407*, 496.
[17] S. B. Yang, X. L. Feng, K. Müllen, *Adv. Mater.* **2011**, *23*, 3575.
[18] J. W. Seo, Y. W. Jun, S. W. Park, H. Nah, T. Moon, B. Park, J. G. Kim, Y. J. Kim, J. Cheon, *Angew. Chem. Int. Ed.* **2007**, *46*, 8828.
[19] T. Bhardwaj, A. Antic, B. Pavan, V. Barone, B. D. Fahlman, *J. Am. Chem. Soc.* **2010**, *132*, 12556.
[20] S. B. Yang, Y. Sun, L. Chen, Y. Hernandez, X. L. Feng, K. Müllen, *Sci. Rep.* **2012**, *2*, 427.
[21] L. Taberna, S. Mitra, P. Poizot, P. Simon, J. M. Tarascon, *Nat. Mater.* **2006**, *5*, 567.
[22] H. L. Wang, L. F. Cui, Y. A. Yang, H. S. Casalongue, J. T. Robinson, Y. Y. Liang, Y. Cui, H. J. Dai, *J. Am. Chem. Soc.* **2010**, *132*, 13978.
[23] K. Chang, W. X. Chen, *ACS Nano* **2011**, *5*, 4720.
[24] K. Chang, W. X. Chen, *J. Mater. Chem.* **2011**, *21*, 17175.
[25] S. B. Yang, X. L. Feng, L. Wang, K. Tang, J. Maier, K. Müllen, *Angew. Chem. Int. Ed.* **2010**, *49*, 4795.
[26] D. H. Wang, D. W. Choi, J. Li, Z. G. Yang, Z. M. Nie, R. Kou, D. H. Hu, C. M. Wang, L. V. Saraf, J. G. Zhang, I. A. Aksay, J. Liu, *ACS Nano* **2009**, *3*, 907.
[27] Y. S. Tao, M. Endo, K. Kaneko, *J. Am. Chem. Soc.* **2009**, *131*, 904.
[28] K. X. Sheng, Y. Q. Sun, C. Li, W. J. Yuan, G. Q. Shi, *Sci. Rep.* **2012**, *2*, 247.
[29] S. B. Yang, Y. J. Gong, Z. Liu, L. Zhan, D. P. Hashim, L. L. Ma, R. Vajtai, P. M. Ajayan, *Nano Lett.* **2013**, *13*, 1596.